Published in final edited form as:
J Mech Behav Biomed Mater. 2013 December ; 28: 26–36. doi:10.1016/j.jmbbm.2013.07.016.

The impact of discrete compartments of a multi-compartment collagen-GAG scaffold on overall construct biophysical properties

D.W. Weisgerber[a], **D.O. Kelkhoff**[a], **S.R. Caliari**[b], and **B.A.C. Harley**[b,c,*]

[a]Department of Materials Science and Engineering, University of Illinois at Urbana-Champaign, Urbana, IL 61801, USA

[b]Department of Chemical and Biomolecular Engineering, University of Illinois at Urbana-Champaign, Urbana, IL 61801, USA

[c]Institute for Genomic Biology, University of Illinois at Urbana-Champaign, Urbana, IL 61801, USA

Abstract

Orthopedic interfaces such as the tendon-bone junction (TBJ) present unique challenges for biomaterials development. Here we describe a multi-compartment collagen–GAG scaffold fabricated via lyophilization that contains discrete mineralized (CGCaP) and non-mineralized (CG) regions joined by a continuous interface. Modifying CGCaP preparation approaches, we demonstrated scaffold variants of increasing mineral content (40 vs. 80 wt% CaP). We report the impact of fabrication parameters on microstructure, composition, elastic modulus, and permeability of the entire multi-compartment scaffold as well as discrete mineralized and non-mineralized compartments. Notably, individual mineralized and non-mineralized compartments differentially impacted the global properties of the multi-compartment composite. Of particular interest for the development of mechanically-loaded multi-compartment composites, the elastic modulus and permeability of the entire construct were governed primarily by the non-mineralized and mineralized compartments, respectively. Based on these results we hypothesize spatial variations in scaffold structural, compositional, and mechanical properties may be an important design parameter in orthopedic interface repair.

Keywords

Collagen scaffold; Multi-compartment; Mineral interface; Biophysical properties

1. Introduction

Spatially-organized tissues such as the tendon-bone junction (TBJ) provide unique challenges for the development of tissue engineering and regenerative medicine solutions. The TBJ is the anatomical solution for connecting relatively compliant tendon to stiffer ($E_{bone} \sim 10^2 \times E_{tendon}$) bone, using graded interfacial zone with overlapping patterns of microstructural and biochemical cues to connect these two tissue compartments (Genin et

*Correspondence to: Department of Chemical and Biomolecular Engineering, Institute for Genomic Biology, University of Illinois at Urbana-Champaign, 110 Roger Adams LaboratoryUrbana, 600 S. Mathews Ave., IL 61801, USA. Tel: +1 217 244 7112; fax: +1 217 333 5052. bharley@illinois.edu (B.A.C. Harley).

al., 2009; Thomopoulos et al., 2010). Despite this mechanically efficient design, the insertion region remains a common site of injury (Woo et al., 2000; Wopenka et al., 2008), with more than seventy-five thousand reconstructive surgeries per year in the US (Butler et al., 2008; Vitale et al., 2007). However, high rates of interface re-tear after surgical reattachment (Boileau et al., 2005; Galatz et al., 2007; Klepps et al., 2004; Millar et al., 2009) motivate the development of a multi-compartment biomaterial containing distinct tendinous and osseous compartments connected by a gradient interface. Such a material might be expected to drive multi-lineage stem cell differentiation or alternatively support the bioactivity of multiple differentiated cells in a spatially-selective manner. However, while the need for multicompartment biomaterials is compelling, it is unclear how inducing spatial gradations in matrix architecture and mineral content might affect the overall behavior of the final composite.

While gradient or multi-compartment biomaterials offer an avenue to explore regenerative repair of orthopedic interfaces, critical questions remain regarding both appropriate methods to fabricate and characterize key properties of a graded biomaterial. A wide range of fabrication methods may be applicable for creating spatially-graded biomaterials for orthopedic insertions, including: sequential dipping into mineralizing solutions (Li et al., 2009), co-electrospinning multiple polymer precursor solutions (Nerurkar et al., 2010), stereolithography and 3D–printing technologies (Chan et al., 2010; Feinberg et al., 2001; Smith et al., 2007), and layering hydrogel constructs (Khanarian et al., 2012; Moffat et al., 2009). Our efforts have concentrated on lyophilization approaches to create spatially-graded collagen–glycosaminoglycan (CG) scaffolds. A highly porous (>95%) sponge-like material with interconnected pores defined by CG fibers, termed struts, CG scaffolds have previously been used for a variety of regenerative medicine application including dermis, peripheral nerves, cartilage (Harley et al., 2004; Yannas, 2001; Yannas et al., 1989), and most recently tendon (Caliari and Harley, 2011; Caliari et al., 2011). Mineralized variants of these scaffolds (CGCaP) have recently been described (Harley et al., 2010a; Kanungo and Gibson, 2009b; Kanungo et al., 2008; Lynn et al., 2010), where nanocrystallites of calcium phosphate are introduced within the CG content.

Recently, Harley et al., 2010b described a fabrication method based on layering distinct CG and CGCaP suspension prior to lyophilization to create multi-compartment CG scaffolds containing distinct CG and CGCaP regions linked by a continuous interface. Originally developed for osteochondral tissue engineering applications (Getgood et al., 2012), our goal is to develop an improved understanding of how the local microstructural and mechanical properties of the discrete compartments within this multi-compartment material impact its overall behavior. Such studies are of particular importance for development of mechanically-loaded (in vivo, in vitro) biomaterials as non-uniformities across the material may alternatively magnify or shield distinct regions from the effects of loading. This manuscript describes microstructural, mechanical, and permeability properties of the discrete scaffold compartments as well as how the overall properties of the multi-compartment scaffold are impacted by its spatially-heterogeneous structure.

2. Materials and methods

2.1. Fabrication of scaffolds

2.1.1. Fabrication of CG and CGCaP precursor suspensions—CG scaffolds were fabricated from a suspension consisting of 0.5 w/w% type I collagen from bovine Achilles tendon (Sigma-Aldrich, St. Louis, MO) and 0.044 w/w% chondroitin sulfate from shark cartilage (Sigma-Aldrich, St. Louis, MO) in 0.05 M acetic acid (Dagalakis et al., 1980; O'Brien et al., 2005; Yannas, 1992; Yannas et al., 1980, 1989). CGCaP suspensions included the same collagen and chondroitin sulfate components as well as calcium salts ($Ca(OH)_2$,

$Ca(NO_3)_2•4H_2O$, Sigma-Aldrich, St. Louis, MO) in phosphoric acid (Sigma-Aldrich, St. Louis, MO) (Lynn et al., 2010). A titrant-free concurrent mapping method was utilized to generate suspensions with expected 40 wt% and 80 wt% CaP content (Lynn et al., 2010). CG and CGCaP suspensions were degassed and stored at 4 °C prior to lyophilization.

2.1.2. Fabrication of monolithic CG and CGCaP scaffolds—Monolithic (CG, CGCaP) scaffolds were fabricated via lyophilization of the precursor suspensions in a Genesis freeze-dryer (VirTis, Gardiner, NY) using a custom polysulfone array mold containing cylindrical wells (12 mm deep, 13 mm diameter, 1.5 mm thick base). The CG and CGCaP suspensions were cooled at a constant rate of 1 °C/min to a final freezing temperature of −10 °C or −40 °C using methods previously described (O'Brien et al., 2004, 2007). The suspensions were maintained at the final freezing temperature (−10, −40 °C) for 175 min and then sublimated at 0 °C and 200 mTorr to remove ice crystals, resulting in dry, porous monolithic CG or CGCaP scaffolds (O'Brien et al., 2005). CG scaffold variants then underwent a dehydrothermal crosslinking and sterilization step at 105 °C for 24 h in a vacuum oven (Welch, Niles, IL) at <25 Torr (Yannas et al., 1989). Microstructural, mechanical, and compositional analyses were performed using scaffold disks (12 mm diameter, 10 mm height).

2.1.3. Fabrication of multi-compartment CG–CGCaP scaffolds—Multi-compartment CG–CGCaP scaffolds were fabricated by layering both CG and CGCaP precursor suspensions prior to lyophilization (Harley et al., 2010b). Briefly, a 1:1 v/v ratio of CG:CGCaP suspensions were layered into the polysulfone array mold and given a period of 20 min for suspension interdiffusion. Following interdiffusion, the layered suspensions were then lyophilized under the same conditions as the monolithic CG and CGCaP scaffolds (2.1.2).

2.1.4. Analysis of monolithic and multi-compartment CG scaffolds—Monolithic and multi-compartment scaffolds were subjected to a battery of biophysical tests. In total, seven distinct CG scaffold variants were fabricated and tested (Table 1). *Monolithic CG scaffolds*: two non-mineralized scaffold variants (CG) were fabricated at freezing temperatures (−10 °C, −40 °C), previously shown to produce significantly different pore sizes when using large stainless steel pans (O'Brien et al., 2005), pore size (2.3), mechanical properties (2.5), and permeability (2.6) were compared between these groups to determine if freezing conditions impacted scaffold properties when using individual polysulfone wells. *Monolithic CGCaP scaffolds*: two 80 wt% mineralized scaffold variants (CGCaP) were also produced at the same freezing conditions (−10 °C, −40 °C) for pore size (2.3), mechanical (2.5), and permeability (2.6) analyses; comparisons were made for effects of freezing temperature (−10 vs. −40 °C) or addition of mineral (vs. monolithic CG scaffolds).

Additionally, a third mineralized scaffold (40 wt%) was also produced at a freezing temperature of −10 °C to demonstrate control over CaP wt% within the final CGCaP scaffold construct; here, compositional analysis (2.4) was performed on 40wt% and 80 wt% CGCaP scaffolds produced at a single freezing temperature (−10 °C). *Multi-compartment CG-CGCaP scaffolds*: two multi-compartment scaffold variants were fabricated from layered CG (top) and 80 wt% CGCaP (bottom) suspensions at identical freezing temperatures (−10 °C, −40 °C) used to create monolithic CG and CGCaP scaffolds. Scaffold pore size and mechanical property analyses were performed on both variants and compared to results from monolithic scaffold at each freezing temperature. Due to the large number and size of the specimens required for permeability testing (2.6), permeability analysis was only performed for one variant (fabricated at −40 °C) while the other scaffold variant (−10 °C) was used for SEM and microCT analyses (2.2) to identify the width of the mineral gradient between CG and CGCaP scaffold compartments. Groups were chosen to identify

how scaffold design properties (freezing temperature, mineral content, addition of a second scaffold compartment) impacted key performance metrics of CG scaffolds previously shown to impact cell bioactivity (Farrell et al., 2006; Harley et al., 2007, 2008b; Harley et al., 2007; Haugh et al., 2010; O'Brien et al., 2005, 2007).

2.2. SEM and microCT analysis

Microstructural features of the multi-compartment scaffolds were imaged using scanning electron microscopy (SEM) and micro-computed tomography (microCT) (Table 1). SEM analysis was performed with a JEOL JSM-6060LV Low Vacuum Scanning Electron Microscope (JEOL USA, Peabody, MA) as previously described (Harley et al., 2010b). MicroCT analysis was performed with an Xradia MicroXCT-400 (Xradia, Pleasanton, CA) at 25 keV and 5 W with 1021 projections and a voxel size of 20 μm. A square ROI (7.56 × 7.68 mm^2) was selected and projected throughout the z-stack of images (400 in total). The resulting matrix (7.56 × 7.68 × 8 mm^3) was then processed to determine the width of the graded scaffold region (interface) between the CG and CGCaP compartments. Briefly, each z-stack slice (image) through the scaffold was parsed into a grid of 225 equally-sized square sections (size: 0.25 mm^2, 25 × 25 voxel squares) so as to sample the microCT signal intensity from regions significantly larger than the mean scaffold pore size. The intensity of all 225 section profiles was determined, creating 225 intensity versus z-position profiles per slice. Z-slices possessing an average intensity in between the mean ±3 STD of the first image slice (taken to be pure CGCaP compartment) and the last image slice (taken to be pure CG compartment) were considered part of the interfacial region.

2.3. Microstructural analysis of CG scaffold variants

Microstructural analysis of CG, CGCaP, and CG–CGCaP scaffolds (Table 1) was performed via previously established stereology methods (O'Brien et al., 2004). Briefly, 6 mm diameter samples were cut from the bulk scaffold specimens using a biopsy punch (Integra Miltex, York, PA), embedded in glycomethacrylate (Polysciences Inc., Warrington, PA), and subsequently sectioned (5 μm slices) in both the transverse and longitudinal planes. After staining for collagen with aniline blue (Thermo Fisher Scientific Inc, Waltham, Ma), histology specimens were imaged using an optical microscope (Leica Microsystems, Wetzlar, Germany). Image analysis was then performed using a linear intercept macro within Scion Image, calculating pore size and pore aspect ratio (O'Brien et al., 2004, 2005).

2.4. Compositional analysis of CGCaP scaffolds

The relative fractions of collagen, GAG and CaP components of the CGCaP scaffold variants (Table 1) were determined from a hydroxyproline assay to measure collagen content (Samuel, 2009), a 1,9-dimethylmethylene blue (DMMB) assay to measure GAG content (Barbosa et al., 2003), and subsequent mass subtraction to determine the remaining CaP fraction (Harley et al., 2010a; Lynn et al., 2010). Briefly, the hydroxyproline assay was performed after digesting samples in 6 M HC1 (Sigma-Aldrich, St. Louis, MO) at 110 °C for 24 h using a fluorometer (Tecan, Männedorf, Switzerland) to compare experimental results to a standard curve of hydroxyproline concentrations to quantify the collagen content in each scaffold variant. Scaffold GAG content was similarly measured via a DMMB assay after digesting scaffold samples in proteinase K (Sigma-Aldrich, St. Louis, MO) overnight at 56 °C; following isolation, the disassociated DMMB content was quantified via a fluorometer and compared to a standard curve of GAG content. CaP fraction was then determined as the remaining dry mass of the samples (Harley et al., 2010a; Lynn et al., 2010). The mineral phase of the CaP content was determined via X-ray diffraction (XRD) analysis (Harley et al., 2010a, 2010b; Lynn et al., 2010) using a Siemens/Bruker D-5000 diffractometer (Bruker AXS, Madison, WI) with a Cu Kα from 2.5° 2θ to 50° 2θ at a rate of

1°/min with an increment of 0.1° 2θ. The resulting spectra were analyzed using MDI Jade (Materials Data Inc., Livermore, CA).

2.5. Mechanical analysis of collagen scaffolds

Given that surgical placement of a biomaterial for TBJ repair is likely to place the material under compressive load, we examined the behavior of our scaffold variants (Table 1) under compressive load. Compression tests were performed on dry scaffold specimens using an MTS Insight Electromechanical load frame (MTS, Eden Prairie, MN) with a 250 N load cell. Samples (both single compartment or multi-compartment) were axially compressed to 75% of their total height at a rate of 1 mm/min (Harley et al., 2007). Both the height and diameter of each scaffold specimen was determined using calipers prior to mechanical testing. Resultant stress–strain plots were analyzed to determine scaffold linear elastic modulus (E^*), taken from the linear elastic regime of the scaffolds (Harley et al., 2007), as well as collapse strain ε^*_{el} and stress σ^*_{el}, taken from the intersection of the linear regressions from the linear elastic and collapse plateau regimes (Harley et al., 2007), which behave as low-density, open-cell foams (Gibson et al., 2010).

2.6. Analysis of scaffold permeability

The axial permeability of each scaffold variant (Table 1) under axial compression was determined using a custom polycarbonate rig previously described (O'Brien et al., 2007). Briefly, hydrated scaffold specimens (10 mm thick, 12 mm diameter) were compressed between two T316 stainless steel mesh disks (0.0075” wire diameter, 0.009” gaps, TWP Inc, Berkley, CA) separated by a series of rubber gaskets and polycarbonate spacers to generate distinct levels of applied strain (ε: 0, 10, 40, 65%). The resultant flow rate (Q) of deionized water with viscosity (μ) under a defined pressure head (ΔP: 1.2”, 3.0”, or 7” depending on the scaffold variant and degree of compression) through the scaffold (thickness, 1; cross-sectional area, A) was measured in small volumes using a graduated cylinder (10 ± 0.1 mL) and timer. The permeability (K) was then calculated as previously described for collagen scaffolds via Darcy's law (O'Brien et al., 2007):

$$\mathrm{K}=\frac{Ql\mu}{\Delta \mathrm{PA}}$$

2.7. Statistics

One-way or two-way (independent factors: freezing temperature, scaffold mineralization) analysis of variance (ANOVA) was applied to microstructural, permeability, and mechanical results followed by Tukey-HSD post-hoc tests. Significance was set at $p<0.05$. Mean pore size analysis was calculated using 24 images from $n = 2$ longitudinal and $n = 2$ transverse scaffold specimens for monolithic CG and CGCaP scaffolds. Stereological analysis of each compartment and the interface of CG–CGCaP scaffolds was analyzed using $n = 2$ samples.

A minimum of $n = 6$ (per scaffold type) and $n = 3$ (per degree of compression and scaffold type) samples were analyzed for mechanical characterization and permeability studies, respectively. Error is reported in figures as the standard deviation (STD) of the mean unless otherwise noted.

3. Results

3.1. SEM and microCT analysis of multi-compartment CG–CGCaP scaffolds

The shift in SEM micrograph signal intensity across the multi-compartment CG–CGCaP (80 wt%) scaffolds indicates distinct CGCaP and CG regions (Fig. 1). Analysis of the signal

intensity from microCT identified distinct non-mineralized (CG) and mineralized (80 wt% CGCaP) compartments along with an approximate interface width, 1.92 ± 0.66 mm (Fig. 1).

3.2. Microstructural analysis of single and multicompartment scaffolds

While freezing temperature has been previously shown to be an important design parameter for CG scaffolds made as sheets in aluminum and stainless steel molds (O'Brien et al., 2004, 2007), freezing temperature was not observed to have a statistically significant impact on scaffold microstructure when scaffolds were fabricated in individual polysulfone wells (Fig. 2, Table 2). Notably, no effect of freezing temperature was found on scaffold pore size within CG and CGCaP groups (−10 °C vs. −40 °C) comparison; interestingly, CGCaP scaffolds displayed non-significantly reduced pore size compared to CG scaffolds fabricated at the identical freezing conditions. For multi-compartment scaffolds fabricated at −10 °C, the reduction in pore size in the mineralized compartment versus the interface region and non-mineralized compartment was significant ($p<0.05$), supporting the conclusion that suspension composition significantly impacts final scaffold structure.

3.3. Compositional analysis of CGCaP scaffold variants

Compositional analysis confirmed the relative ratio of collagen, GAG, and mineral content for two CGCaP scaffold variants matched that expected based on fabrication parameters. Notably, the 40 wt% CGCaP scaffolds ($n = 4$) were found to contain 37.8 ± 1.1 wt% collagen, 19.7 ± 0.4 wt% GAG, and 42.6 ± 1.2 wt% CaP mineral. 80 wt% CGCaP scaffold variants ($n = 4$) were found to contain 18.6 ± 3.0 wt% collagen, 2.9 ± 0.2 wt% GAG, and 78.5±3.0 wt% CaP mineral. Subsequent XRD analysis identified the CaP mineral phase in both 40 wt% and 80 wt% variants to be composed entirely of brushite (Fig. 3), in agreement with previous studies (Harley et al., 2010a; Lynn et al., 2010).

3.4. Mechanical behauior of single and multicompartment scaffolds

Single-compartment CG and CGCaP scaffolds as well as multicompartment scaffold variants all behaved as low-density, open-cell foams in compression. As CG, 80 wt% CGCaP, and 80 wt% multi-compartment scaffolds fabricated at both −10 °C and −40 °C displayed characteristic linear elastic, collapse plateau, and *densification* regimes, stress–strain curves are presented only for the three variants fabricated at −40 °C (Fig. 4A), though mechanical properties are reported for CG, 80 wt% CGCaP, and 80 wt% CG–CGCaP scaffold variants (Table 3). Elastic moduli were determined from the linear elastic regime (ε: 0.02–0.12) as a function of freezing conditions (T_f −10 °C and −40 °C) and scaffold composition (CG, CGCaP, CG–CGCaP) (Table 3, Fig. 4B). Statistically significant ($p<0.05$) differences in moduli were observed between the CG, CGCaP and CG–CGCaP scaffolds for each freezing temperature, with the exception of CG and CG–CGCaP at −40 °C; additionally a statistically significant ($p<0.05$) influence of freezing temperature (−10 °C vs. −40 °C) was also observed for CGCaP samples. While some statistically significant differences were observed between the calculated collapse strains ε_{el}^{*} for all variants (CG, CGCaP, CG–CGCaP), all collapse stains were found to be approximately 0.1 (range: 0.07–0.14; Table 3), consistent with expectations for low-density, open cell foams (Gibson et al., 2010; Harley et al., 2007). As a product of collapse strain and elastic moduli, statistically significant differences were not-surprisingly also observed in collapse stress σ_{el}^{*} between CG, CGCaP, and multi-compartment CG–CGCaP scaffolds in a pattern consistent with the observed differences in elastic moduli (Table 3).

3.5. Permeability of single and multi-compartment CG scaffolds

The permeability of each scaffold variant was determined as a function of applied compressive strain via a constant head permeability test (Table 4, Fig. 5) (O'Brien et al.,

2007). For clarity, normalized permeability (k/k_o) is reported for each variant where scaffold permeability at a given applied strain (ε: 0, 10, 40, 65%) was normalized against that of the non-compressed scaffold (ε: 0%)(Fig. 5). Notably, permeability results for unstrained scaffolds indicate that the stiffer CGCaP variants maintained a higher permeability than the softer CG and CG–CGCaP variants (Table 4). Permeability of all scaffold variants (CG; 80 wt% CGCaP; 80 w% multi-compartment scaffold) decreased significantly ($p<0.05$) with applied compression (Fig. 5). In addition to empirical results, predicted changes in scaffold permeability with mechanical load were calculated via previously described defined cellular solids methods (Fig. 5, Theory) (Gibson, 1997; O'Brien et al., 2007) to facilitate comparisons of distinct scaffold variants.

4. Discussion

Orthopedic interface injuries inspired the creation of a multicompartment CG–CGCaP scaffold to mimic elements of the junction between bone and soft tissue (e.g., tendon, cartilage, ligament). Careful microstructural (O'Brien et al., 2004, 2005, 2007), mechanical (Harley et al., 2007), and biophysical (Harley et al., 2008a) characterization of single-compartment CG materials as well as a lyophilization approach to create multi-compartment CG scaffolds (Harley et al., 2010b) has been described. However, the influence of multiple scaffold compartments on overall construct biophysical properties has not been explored. Here we hypothesized that the addition of a second scaffold compartment would have a significant impact on both scaffold microstructural properties and biophysical performance.

This investigation used a polysulfone mold containing individual wells (12 mm diameter) to create single scaffold specimens per well, as opposed to previous efforts which concentrated on creating larger scaffold sheets using stainless steel pans (O'Brien et al., 2005). Selected for ease of rapid machining, we also explored whether the reduced thermal conductivity of the polysulfone (vs. stainless steel) mold still enabled control over final scaffold pore size via solidification temperature (−10 °C, −40 °C) during lyophilization (O'Brien et al., 2005). While the interdiffusion time allowed during fabrication of multi-compartment scaffolds may also impact interface properties, for this investigation we chose a single interdiffusion condition sufficient to create a distinct interfacial zone large enough for microstructural characterization (Fig. 1). Consistent with previously reported multicompartment CG scaffolds (Harley et al., 2010b), microCT and SEM analysis showed two distinct (CG, CGCaP) scaffold compartments linked with a continuous interface devoid of signs of delamination (Fig. 1). MicroCT was further employed to determine the distribution of mineral content through the depth of the CG–CGCaP scaffolds, identifying an upper bound for the interface width (1.9±0.7 mm) (Fig. 1C). Ongoing work is examining a wider range of interdiffusion conditions and layering geometries to explore further manipulations of the interface width and geometry.

The influence of lyophilization conditions on microstructural, mechanical, and biophysical properties of CG (Harley et al., 2007; Kanungo and Gibson, 2009a; O'Brien et al., 2004, 2005, 2007) and CGCaP scaffolds (Harley et al., 2010a; Kanungo and Gibson, 2009b; Kanungo et al., 2008), and in a more limited manner for multi-compartment CG–CGCaP scaffolds (Getgood et al., 2012; Harley et al., 2010b), has been previously reported for large sheets of material. To facilitate future multiplex scaffold analyses approaches, we created individually sized scaffold disks in a custom polysulfone mold array. As lyophilization depends on heat transfer to create the final scaffold structure, it is likely that decreasing the mold size to create single scaffold samples has significantly changed the effect of processing conditions on final scaffold properties. Notably, while freezing temperature has previously been shown to significantly impact the scaffold microstructure (Haugh et al., 2010; O'Brien et al., 2005), here we observed only a non-significant trend of decreasing pore size with

decreasing freezing temperature (−10 °C to −40 °C) and increasing suspension density (CG to CGCaP) (Fig. 2, Table 2). Given the known solidification kinetics of the precursor CG suspensions (O'Brien et al., 2004; O'Brien et al., 2005), this result is alternatively not surprising and informative. It is likely that the smaller suspension volume as well as the reduced thermal conductivity of the individual polysulfone molds used here blunted any differences in suspension undercooling (−5 to −9 °C), ice crystal nucleation, and subsequent coarsening events during scaffold fabrication despite the use of disparate freezing temperatures (−10 °C, −40 °C). Ongoing efforts are exploring the complex relationship between suspension volume, mold thermal conductivity, and freezing kinetics (freezing rate, final temperature) to identify the critical point where a reduction in suspension volume or mold thermal conductivity does not result in a discernible change in scaffold microstructural properties. However, here we determined that final freezing temperature had negligible effect on resultant scaffold structural properties using the new individual well mold design used here (1.5 mm thick polysulfone base; individual wells: 12 mm deep, 13 mm diameter).

Interestingly, we also found that suspension chemistry can significantly impact compartment microstructure in multi-compartment scaffolds in unexpected ways. Notably, we observed a significant increase in the final pore size of the non-mineralized layer of the multi-compartment scaffold vs. the monolithic CG scaffold fabricated from the identical suspension (Fig. 2, Table 2). The increase in pore size suggests that solidification of the CG layer was slowed in the multicompartment scaffold format. As multi-compartment scaffolds are fabricated by layering two suspensions prior to lyophilization, this result suggests that differences in internal heat transfer coefficients of the suspensions are likely responsible for the increased pore size of the non-mineralized scaffold compartment. With conductive heat transfer through the mold previously identified as being primarily responsible for determining scaffold pore size, the relative position of CG and CGCaP suspensions has the potential to significantly impact both compartments. Here, the pore size of the CG compartment of the multicompartment scaffold was significantly larger than that of monolithic CG suspension. This effect was enhanced for the suspension temperature (−10 °C) with the longest solidification times (O'Brien et al., 2005) though there was not a significant increase in pore size of the mineralized compartment. These results suggest that reduced heat transfer through the higher density CGCaP suspension was extending the solidification of the CG suspension, most significantly in the case of a freezing profile already designed to lead to slowed solidification. With the CG suspension layered on top of the CGCaP compartment to fabricate the final composite, this results suggests that heat transfer coefficients of the CG suspensions themselves may become a critical design parameter in future endeavors.

In addition to quantifying the influence of scaffold chemistry and freezing conditions on final scaffold microstructure, we also confirmed CGCaP variants could be produced with defined mineral content and phase. Notably, two CGCaP variants that span the physiological range of CaP wt% in bone (33–71 wt%) (Bloebaum et al., 1997; Pietrzak and Woodell-May, 2005; Sierpowska et al., 2007; Yeni et al., 1998) were validated (40 and 80 wt%) Gleeson et al., 2010. These results were in good agreement with predictions made via previously described concurrent mapping approach (Harley et al., 2010a; Lynn et al., 2010) to predict CaP wt% as a function of suspension phosphoric acid and calcium salts content. The CaP mineral phase of both the 40 wt% and 80 wt % CGCaP scaffolds was found to consist solely of brushite, consistent with previous studies that showed initially formed brushite could be modified via hydrolysis to octacalcium phosphate and apatite phases (Harley et al., 2010a; Lynn et al., 2010).

The mechanical behavior of the monolithic CG and CGCaP scaffolds as well as the multi-compartment CG–CGCaP scaffolds were investigated in compression (Fig. 4). In all cases,

the stress–strain profiles were characteristic of low-density, open-cell foams possessing linear elastic, collapse plateau, and densification regimes (Gibson et al., 2010). Not surprisingly, the elastic modulus of the non-mineral CG scaffold variants was more than an order of magnitude smaller than the corresponding mineralized CGCaP scaffold variants (Fig. 4, Table 3). As the multi-compartment scaffold samples were not tested in tension, we have not investigated the potential problem of delamination. However, we believe that the lack of defects at the interface post-fabrication as evidenced by SEM and micro-CT suggests a controlled interface width may dictate scaffold delamination. Ongoing efforts are addressing mechanical behavior of these multicompartment scaffolds in tension, particularly as a function of the width and shape of the interface region. Such efforts are part of long-term culture experiments to explore mesenchymal stem cell differentiation as a function of local scaffold biophysical properties.

More interesting was the mechanical performance of the multi-compartment scaffold, which highlighted the likely presence of heterogeneous strain fields within multi-compartment and spatially graded biomaterial (Fig. 4, Table 3). Here, the relatively low elastic modulus of the composite CG–CGCaP scaffold (roughly twice that of the non-mineralized CG scaffold) can be attributed to the majority of scaffold compression in the linear elastic regime (ε: 0.08–0.12) concentrated in the significantly softer CG compartment. Divergence in the stress–strain behavior of the multi-compartment versus the non-mineralized scaffold was not noted until sufficient strain was applied (ε>0.40) to induce densification (Gibson et al., 2010) in the non-mineralized region of the multi-compartment scaffold (Fig. 4). With densification, additional strain would be expected to be transmitted to the relatively-stiffer mineralized compartment, consistent with the differences observed. Additionally, the observed difference (2-fold) in elastic modulus between the multi-compartment and non-mineralized CG scaffolds can be attributed to the calculation of applied strain. While strain was calculated based on the entire thickness of the construct, for the range of strains used to determine elastic modulus (ε: 0.08–0.12), deformation in the multi-compartment scaffold is likely only occurring in the non-mineralized zone. These results highlight the need for improved approaches to characterize spatially-graded biomaterials in order to more rigorously assess the local scaffold microenvironment.

Scaffold permeability also varied as a function of composition, freezing temperature, and applied strain. In the absence of compression (ε: 0%), a significant (p<0.05) influence of scaffold type (CG, CGCaP, and CG–CGCaP) as well as freezing temperature (−10 °C, −40 °C) was observed, suggesting a sensitivity to scaffold composition and pore size (Fig. 2, Table 4). Interestingly, the permeability of the CGCaP scaffold variants was significantly greater than the non-mineralized CG scaffolds (Table 4). While the CGCaP scaffolds are significantly less porous than CG scaffolds due to the added CaP content, increased permeability may be due to reduced scaffold microstructural deformation under the applied pressure head during permeability tests.

A strong dependence of applied strain on scaffold permeability was also observed, with scaffold permeability decreasing significantly (p<0.05) under increasing levels of applied strain for single (CG, CGCaP) and multi-compartment scaffolds (Fig. 5). Changes in permeability with applied compression compared favorably with predictions made using a previously described cellular solids relationship (Fig. 5, dashed lines) based on the mechanics of pore collapse (Gibson and Ashby, 1997), relating CG scaffold permeability (K) to applied strain (ε) (O'Brien et al., 2007):

$$\mathrm{K} \propto (1-\varepsilon)^2$$

Interestingly, there was no significant difference in permeability between non-mineralized CG and multi-compartment scaffolds for applied compressive strains less than 50% (Fig. 4). This behavior suggests that like mechanical behavior, properties of the multi-compartment scaffold are limited by the CG compartment.

5. Conclusions

This work describes the microstructural and mechanical properties of a series of CG, mineralized CGCaP, and multicompartment CG–CGCaP scaffolds for orthopedic interface repair applications. All scaffold variants exhibit mechanical behavior and permeability responses consistent with cellular solids theory, with the limiting compartment primarily defining the behavior of the multi-compartment scaffold. These results highlight the importance of developing strategies for quantifying local microstructural and biophysical properties of spatially heterogeneous materials to aid their optimization for regenerative repair of orthopedic insertion injuries.

Acknowledgments

The authors would like to acknowledge Karen Doty (Veterinary Sciences, UIUC) for sectioning of GMA embedded samples and the IGB Core Facilities for assistance with RT-PCR. DWW was funded at UIUC from National Science Foundation (NSF) Grant 0965918 IGERT: Training the Next Generation of Researchers in Cellular & Molecular Mechanics and BioNanotechnology. We are grateful for funding for this study provided by the Chemistry–Biology Interface Training Program NIH NIGMS T32GM070421 (SRC) as well as the Chemical and Biomolecular Engineering Department and the Institute for Genomic Biology (BAH) at the University of Illinois at Urbana-Champaign. This research was carried out in part in the Frederick Seitz Materials Research Laboratory Central Facilities, University of Illinois, which are partially supported by the U.S. Department of Energy under grants DE-FG02-07ER46453 and DE-FG02-07ER46471.

REFERENCES

Barbosa I, Garcia S, Barbier-Chassefiere V, Caruelle JP, Martelly I, Papy-Garcia D. Improved and simple micro assay for sulfated glycosaminoglycans quantification in biological extracts and its use in skin and muscle tissue studies. Glycobiology. 2003; 13:647–653. [PubMed: 12773478]

Bloebaum RD, Skedros JG, Vajda EG, Bachus KN, Constantz BR. Determining mineral content variations in bone using backscattered electron imaging. Bone. 1997; 20:485–490. [PubMed: 9145247]

Boileau P, Brassart N, Watkinson DJ, Carles M, Hatzidakis AM, Krishnan SG. Arthroscopic repair of full-thickness tears of the supraspinatus: does the tendon really heal. Journal of Bone and Joint Surgery-American. 2005; 87A:1229–1240.

Butler DL, Juncosa-Melvin N, Boivin GP, Galloway MT, Shearn JT, Gooch C, Awad H. Functional tissue engineering for tendon repair: a multidisciplinary strategy using mesenchymal stem cells, bioscaffolds, and mechanical stimulation. Journal of Orthopaedic Research. 2008; 26:1–9. [PubMed: 17676628]

Caliari SR, Harley BA. The effect of anisotropic collagen- GAG scaffolds and growth factor supplementation on tendon cell recruitment, alignment, and metabolic activity. Biomaterials. 2011; 32:5330–5340. [PubMed: 21550653]

Caliari SR, Ramirez MA, Harley BAC. The development of collagen-GAG scaffold-membrane composites for tendon tissue engineering. Biomaterials. 2011; 32:8990–8998. [PubMed: 21880362]

Chan V, Zorlutuna P, Jeong JH, Kong H, Bashir R. Three-dimensional photopatterning of hydrogels using stereolithography for long-term cell encapsulation. Lab Chip. 2010; 10:2062–2070. [PubMed: 20603661]

Dagalakis N, Flink J, Stasikelis P, Burke JF, Yannas IV. Design of an artificial skin. Part III. Control of pore structure. Journal of Biomedical Materials Research. 1980; 14:511–528. [PubMed: 7400201]

Farrell E, O'Brien FJ, Doyle P, Fischer J, Yannas I, Harley BA, O'Connell B, Prendergast PJ, Campbell VA. A collagen-glycosaminoglycan scaffold supports adult rat mesenchymal stem cell

differentiation along osteogenic and chondrogenic routes. Tissue Engineering. 2006; 12:459–468. [PubMed: 16579679]

Feinberg SE, Hollister SJ, Halloran JW, Chu TM, Krebsbach PH. Image-based biomimetic approach to reconstruction of the temporomandibular joint. Cells Tissues Organs. 2001; 169:309–321. [PubMed: 11455128]

Galatz L, Rothermich S, VanderPloeg K, Petersen B, Sandell L, Thomopoulos S. Development of the supraspinatus tendon-to-bone insertion: localized expression of extracellular matrix and growth factor genes. Journal of Orthopaedic Research. 2007; 25:1621–1628. [PubMed: 17600822]

Genin GM, Kent A, Birman V, Wopenka B, Pasteris JD, Marquez PJ, Thomopoulos S. Functional grading of mineral and collagen in the attachment of tendon to bone. Biophysical Journal. 2009; 97:976–985. [PubMed: 19686644]

Getgood AMJ, Kew SJ, Brooks R, Aberman H, Simon T, Lynn AK, Rushton N. Evaluation of early-stage osteochondral defect repair using a biphasic scaffold based on a collagen-glycosaminoglycan biopolymer in a caprine model. The Knee. 2012; 19:422–430. [PubMed: 21620711]

Gibson, LJ.; Ashby, MF. Cellular Solids: Structure and Properties, U.K. 2nd ed.. Cambridge: Cambridge University Press; 1997.

Gibson, LJ.; Ashby, MF.; Harley, BA. Cellular materials in nature and medicine. Cambridge, U.K: Cambridge University Press; 2010.

Gleeson JP, Punkett NA, O'Brien FJ. Addition of hydroxyapatite improves stifness, interconnectivity and osteogenic potential of a highly porous collagen-based scaffold for bone tissue regeneration. European Cells and Materials. 2010; 20:218–230. [PubMed: 20922667]

Harley BA, Kim HD, Zaman MH, Yannas IV, Lauffenburger DA, Gibson LJ. Microarchitecture of three-dimensional scaffolds influences cell migration behavior via junction interactions. Biophysical Journal. 2008b; 95:4013–4024. [PubMed: 18621811]

Harley BA, Leung JH, Silva EC, Gibson LJ. Mechanical characterization of collagen-glycosaminoglycan scaffolds. Acta Biomaterials. 2007; 3:463–474.

Harley BA, Lynn AK, Wissner-Gross Z, Bonfield W, Yannas IV, Gibson LJ. Design of a multiphase osteochondral scaffold II: fabrication of a mineralized collagen-GAG scaffold. Journal of Biomedical Materials Research Part A. 2010a; 92:1066–1077. [PubMed: 19301274]

Harley BA, Lynn AK, Wissner-Gross Z, Bonfield W, Yannas IV, Gibson LJ. Design of a multiphase osteochondral scaffold III: Fabrication of layered scaffolds with continuous interfaces. Journal of Biomedical Materials Research Part A. 2010b; 92:1078–1093. [PubMed: 19301263]

Harley BA, Spilker MH, Wu JW, Asano K, Hsu HP, Spector M, Yannas IV. Optimal degradation rate for collagen chambers used for regeneration of peripheral nerves over long gaps. Cells Tissues Organs. 2004; 176:153–165. [PubMed: 14745243]

Haugh MG, Murphy CM, O'Brien FJ. Novel freeze-drying methods to produce a range of collagen-glycosaminoglycan scaffolds with tailored mean pore sizes. Tissue Engineering Part C: Methods. 2010; 16:887–894. [PubMed: 19903089]

Kanungo BP, Gibson LJ. Density-property relationships in collagen-glycosaminoglycan scaffolds. Acta Biomaterialia. 2009a; 6:344–353. [PubMed: 19770077]

Kanungo BP, Gibson LJ. Density-property relationships in mineralized collagen-glycosaminoglycan scaffolds. Acta Biomaterialia. 2009b; 5:1006–1018. [PubMed: 19121982]

Kanungo BP, Silva E, Van Vliet K, Gibson LJ. Characterization of mineralized collagen-glycosaminoglycan scaffolds for bone regeneration. Acta Biomaterialia. 2008; 4:490–503. [PubMed: 18294943]

Khanarian NT, Haney NM, Burga RA, Lu HH. A functional agarose-hydroxyapatite scaffold for osteochondral interface regeneration. Biomaterials. 2012; 33:5247–5258. [PubMed: 22531222]

Klepps S, Bishop J, Lin J, Cahlon O, Strauss A, Hayes P, Flatow EL. Prospective evaluation of the effect of rotator cuff integrity on the outcome of open rotator cuff repairs. The American Journal of Sports Medicine. 2004; 32:1716–1722. [PubMed: 15494338]

Li XR, Xie JW, Lipner J, Yuan XY, Thomopoulos S, Xia YN. Nanofrber scaffolds with gradations in mineral content for mimicking the tendon-to-bone insertion site. Nano Letters. 2009; 9:2763–2768. [PubMed: 19537737]

Lynn AK, Best SM, Cameron RE, Harley BA, Yannas IV, Gibson LJ, Bonfield W. Design of a multiphase osteochondral scaffold. I. Control of chemical composition. Journal of Biomedical Materials Research Part A. 2010; 92:1057–1065. [PubMed: 19301264]

Millar NL, Wu X, Tantau R, Silverstone E, Murrell GAC. Open versus two forms of arthroscopic rotator cuff repair. Clinical Orthopaedics and Related Research. 2009; 467:966–978. [PubMed: 19184264]

Moffat KL, Wang IN, Rodeo SA, Lu HH. Orthopedic interface tissue engineering for the biological fixation of soft tissue grafts. Clinical Journal of Sport Medicine. 2009; 28:157–176.

Nerurkar NL, Sen S, Huang AH, Elliott DM, Mauck RL. Engineered disc-like angle-ply structures for intervertebral disc replacement. Spine (Philadelphia Pa, 1976). 2010; 35:867–873.

O'Brien FJ, Harley BA, Waller MA, Yannas IV, Gibson LJ, Prendergast PJ. The effect of pore size on permeability and cell attachment in collagen scaffolds for tissue engineering. Technology and Health Care. 2007; 15:3–17. [PubMed: 17264409]

O'Brien FJ, Harley BA, Yannas IV, Gibson L. Influence of freezing rate on pore structure in freeze-dried collagen-GAG scaffolds. Biomaterials. 2004; 25:1077–1086. [PubMed: 14615173]

O'Brien FJ, Harley BA, Yannas IV, Gibson LJ. The effect of pore size on cell adhesion in collagen-GAG scaffolds. Biomaterials. 2005; 26:433–441. [PubMed: 15275817]

Pietrzak WS, Woodell-May J. The composition of human cortical allograft bone derived from FDA/AATB-screened donors. Journal of Craniofacial Surgery. 2005; 16:579–585. [PubMed: 16077301]

Samuel, CS. Determination of collagen content, concentration, and sub-types in kidney tissue. In: Becker, TDHaGJ., editor. Methods in Molecular Biology. Vol. vol. 466. Totowa, NJ: Humana Press; 2009. p. 223-235.Kidney Research

Sierpowska J, Lammi MJ, Hakulinen MA, Jurvelin JS, Lappalainen R, Toyras J. Effect of human trabecular bone composition on its electrical properties. Medical Engineering and Physics. 2007; 29:845–852. [PubMed: 17097909]

Smith MH, Flanagan CL, Kemppainen JM, Sack JA, Chung H, Das S, Hollister SJ, Feinberg SE. Computed tomography-based tissue-engineered scaffolds in craniomaxillofacial surgery. International Journal of Medical Robotics. 2007; 3:207–216.

Thomopoulos S, Genin GM, Galatz LM. The development and morphogenesis of the tendon-to-bone insertion—what development can teach us about healing. Journal of Musculoskeletal and Neuronal Interactions. 2010; 10:35–45. [PubMed: 20190378]

Vitale MA, Vitale MG, Zivin JG, Braman JP, Bigliani LU, Flatow EL. Rotator cuff repair: an analysis of utility scores and cost-effectiveness. Journal of Shoulder and Elbow Surgery. 2007; 16:181–187. [PubMed: 17399623]

Woo SL, Debski RE, Zeminski J, Abramowitch SD, Saw SS, Fenwick JA. Injury and repair of ligaments and tendons. Annual Review of Biomedical Engineering. 2000; 2:83–118.

Wopenka B, Kent A, Pasteris JD, Yoon Y, Thomopoulos S. The tendon-to-bone transition of the rotator cuff: a preliminary Raman spectroscopic study documenting the gradual mineralization across the insertion in rat tissue samples. Applied Spectroscopy. 2008; 62:1285–1294. [PubMed: 19094386]

Yannas, I. Tissue and Organ Regeneration in Adults. New York: Springer; 2001.

Yannas IV. Tissue Regeneration by use of collagen- glycosaminoglycan copolymers. Clinical Materials. 1992; 9:179–187. [PubMed: 10149968]

Yannas IV, Burke JF, Gordon PL, Huang C, Rubenstein RH. Design of an artificial skin. II. Control of chemical composition. Journal of Biomedical Materials Research. 1980; 14:107–132. [PubMed: 7358747]

Yannas IV, Lee E, Orgill DP, Skrabut EM, Murphy GF. Synthesis and characterization of a model extracellular matrix that induces partial regeneration of adult mammalian skin. Proceedings of the National Academy of Sciences of the United States of America. 1989; 86:933–937. [PubMed: 2915988]

Yeni YN, Brown CU, Norman TL. Influence of bone composition and apparent density on fracture toughness of the human femur and tibia. Bone. 1998; 22:79–84. [PubMed: 9437517]

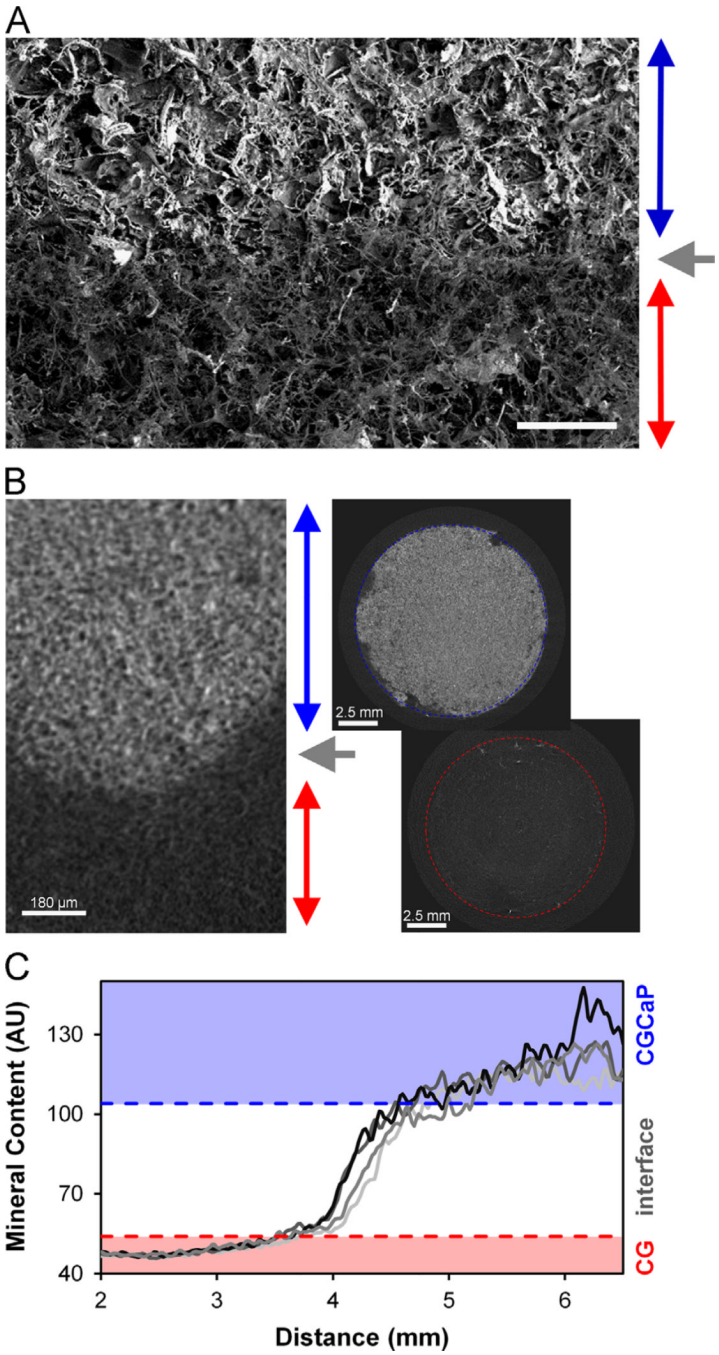

Fig. 1.

(A) SEM image of 80 wt% CG–CGCaP scaffold interface (CGCaP compartment: *blue arrow;* CG compartment: *red arrow*; CG–CGCaP interface: *gray arrow*). Scale bar: 1 mm. (B) Representative microCT image of the multi-compartment scaffold (left); 2D projections taken through the 80 wt% CGCaP (top, right) and CG (bottom, right) scaffold regions. (C) 4 (of 225) line profiles showing the mean pixel intensity (mineral content) across the multi-compartment scaffold. Horizontal dashes lines indicated the upper and lower limits of the 80 wt% CG–CGCaP compartment interfaces (+/−3 STD). X-axis scale refers to absolute position across the multicompartment scaffold relative to the surface of the CG scaffold,

with data presented for mineral content across the interface as well as for ~2 mm of each compartment (CG, CGCaP) on either side. (For interpretation of the references to color in this figure legend, the reader is referred to the web version of this article.)

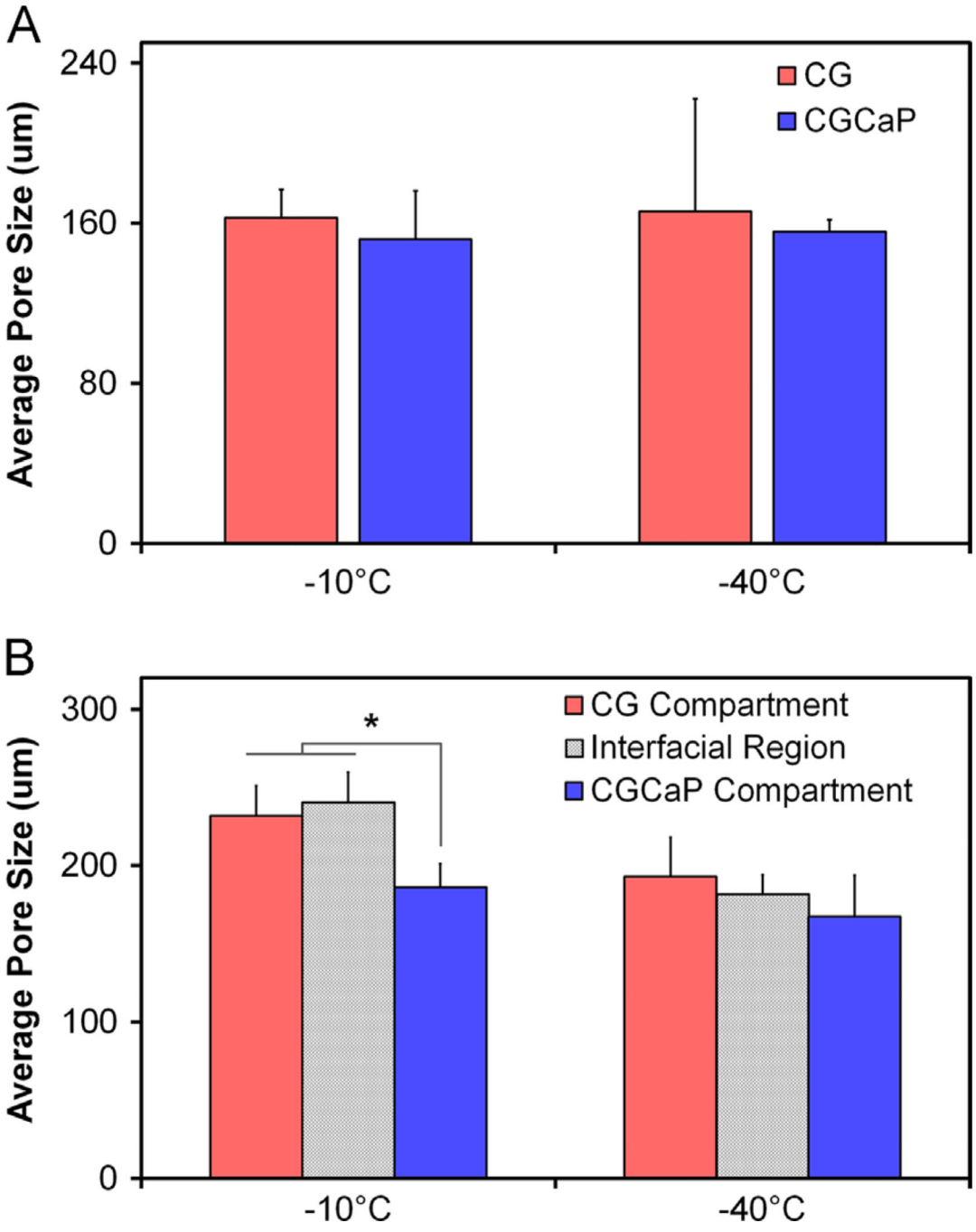

Fig. 2.

(A) Microstructural analysis of CG vs. 80 wt% CGCaP scaffolds as a function of freezing conditions (T_f: −10 °C, −40 °C) indicating a decrease in pore size with scaffold mineralization and a non-significant effect of freezing temperature. (B) Mean pore size of the non-mineralized, interface, and mineralized regions of multi-compartment CG–CGCaP scaffold as a function of freezing temperature. Data expressed as mean±STD, $n = 4$. *$p<0.05$ between CGCaP zone and both the CG and interface zones fabricated at −10 °C.

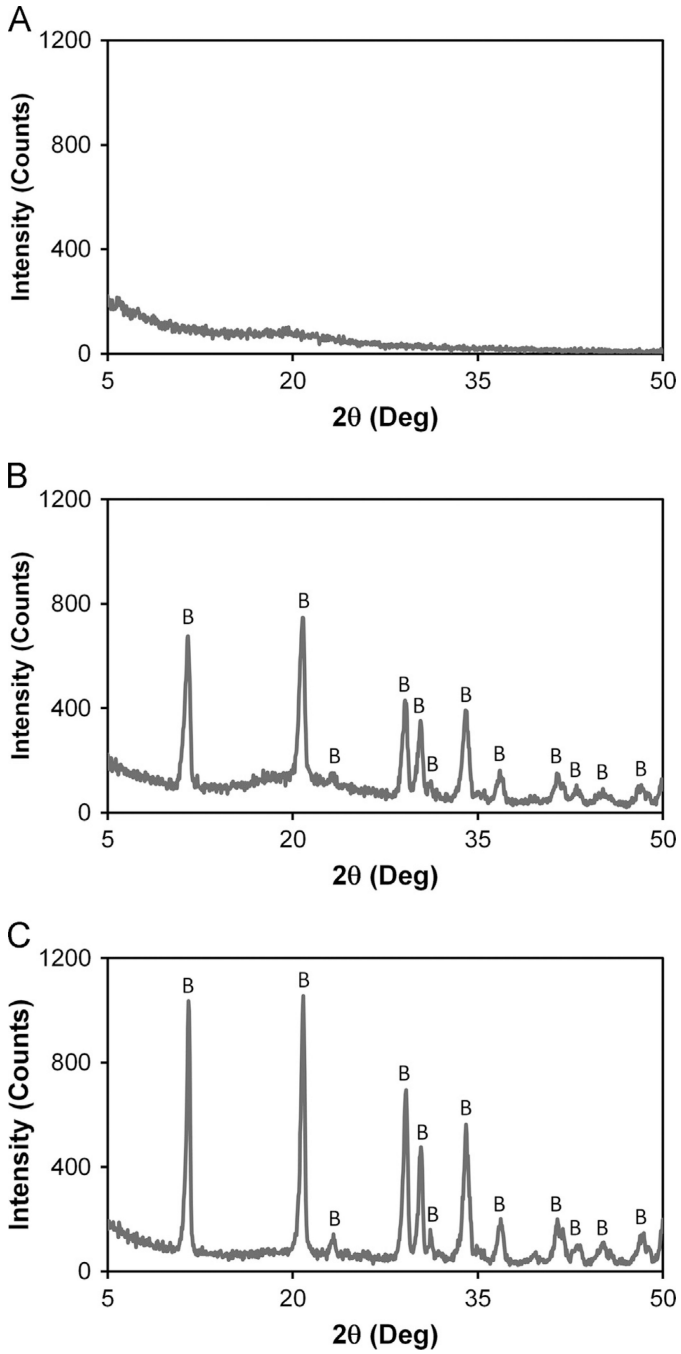

Fig. 3.

XRD analysis of (A) CG, (B) 40 wt%, and (C) 80 wt% CGCaP scaffold variants identifying the predominant form of CaP mineral as brushite (vs. apatite, octacalcium phosphate). Brushite peaks were labeled with ‘B’.

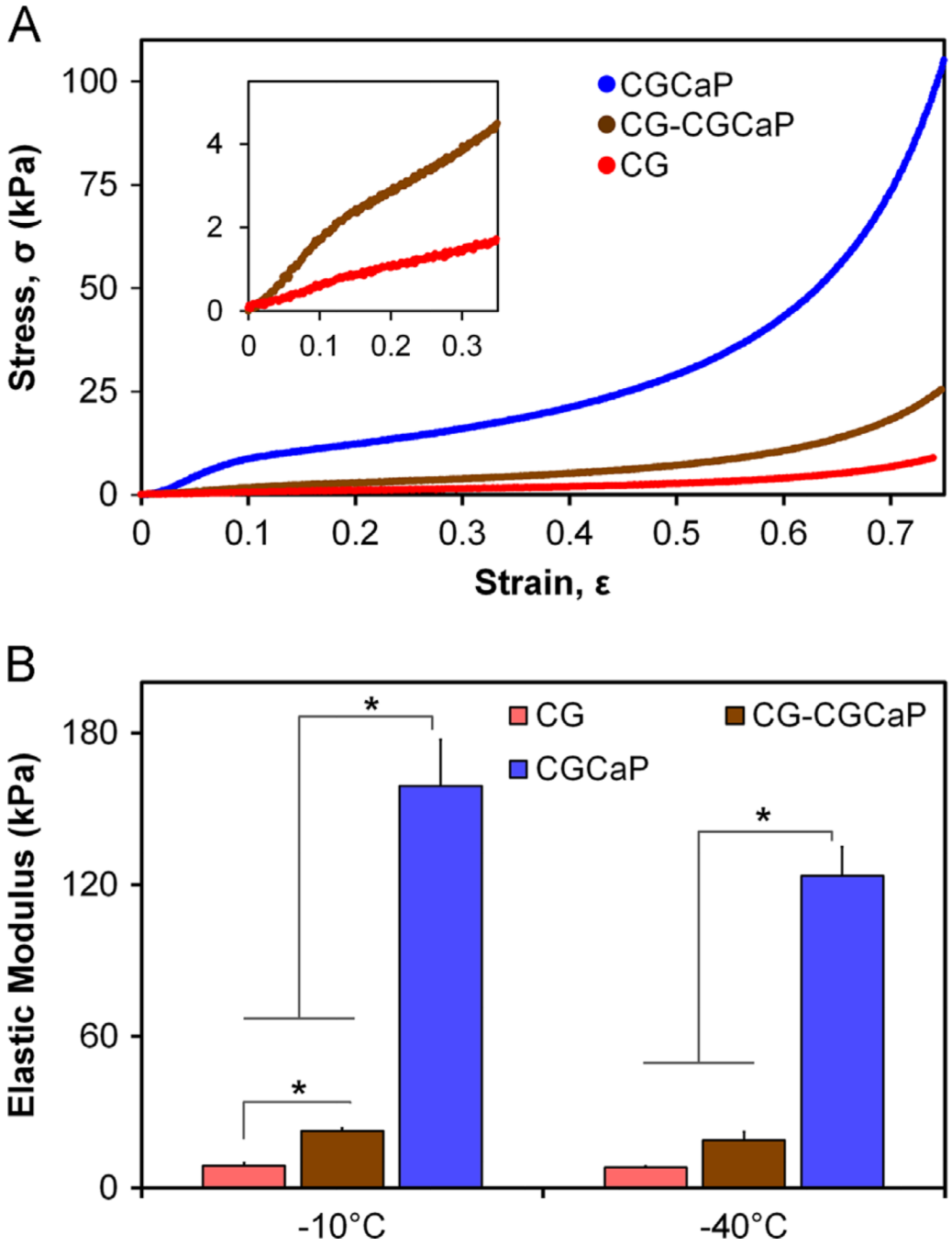

Fig. 4.

(A) CG, 80 wt% CGCaP, and 80 wt% CG–CGCaP scaffolds showed stress–strain behavior in unconfined compression characteristic of low-density open-cell foams, notably distinct linear elastic, collapse plateau, and densification regimes. Inset: magnification of low strain behavior of CG and multi-compartment CG–CGCaP scaffolds. As both −10 °C and −40 °C samples behaved identically, only −40 °C have been presented. (B) The linear elastic moduli of CG, CGCaP, and CG–CGCaP scaffold variants (T_f: −10 °C vs. −40 °C) in compression. Results indicate a significant influence of scaffold composition on compressive modulus. Data expressed as mean±STD, $n = 6$, *$p<0.05$.

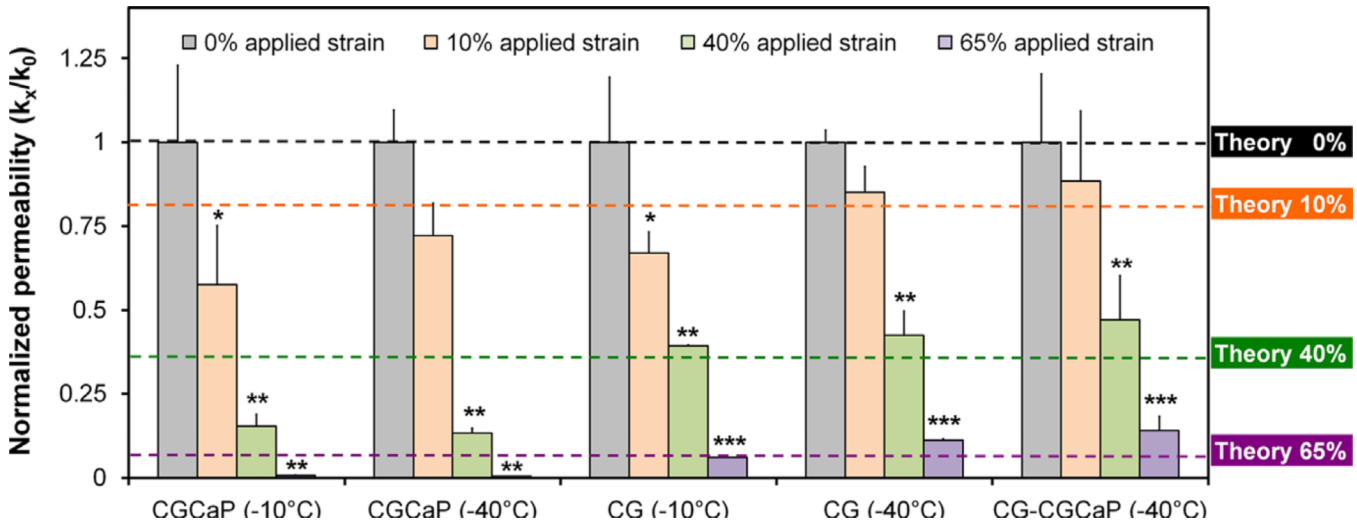

Fig. 5.

Normalized permeability ($k_\varepsilon/k_{\varepsilon=0}$) of CG, 80 wt% CGCaP, 80 wt% CG–CGCaP scaffolds as a function of freezing conditions (T_f: −10 °C, −40 °C) over a range of applied strains (ε: 0, 0.1, 0.4, 0.65). Dashed lines: predicted changes in normalized scaffold permeability as a function of applied strain via a previously described cellular solids model of CG scaffold permeability. Data expressed as mean±STD, n = 3. Significance: *p<0.05 vs. 0% applied strain; **p<0.05 vs. 0% and 10% applied strain; ***p<0.05 vs. 0%, 10%, and 40% applied strain.

Table 1

Summary of scaffold variants produced for biophysical analyses.

Scaffold	Mineral content (wt%)	Freezing temp. (°C)	Tests performed
CG	0	−10	Microstructure; mechanical; permeability
		−40	Microstructure; mechanical; permeability
CGCaP	40	−10	CaPwt%
	80	−10	Microstructure; mechanical; permeability; CaPwt%
		−40	Microstructure; mechanical; permeability
CG–CGCaP	80	−10	Microstructure; mechanical; interface width
		−40	Microstructure; mechanical; permeability

Table 2

Mean pore size and aspect ratios of single compartment CG and 80 wt% CGCaP, and 80 wt% multi-compartment CG–CGCaP (CG, interface, CGCaP regions). Results reported as mean±STD with histology sections taken from $n = 4$ and $n = 2$ specimens for single-compartment and multi-compartment scaffolds, respectively.

		T_f −10 °C		T_f −40 °C	
		Pore size (μm)	**Pore aspect ratio**	**Pore size (μm)**	**Pore aspect ratio**
Single	CG	163±14	0.92±0.03	166±56	0.92±0.03
	CGCaP	152±24	0.94±0.02	156±6	0.95±0.01
Multi	CG	232±20*	0.93±0.02	193±25	0.94±0.02
	Interface	240±19*	0.94±0.02	181±13	0.92±0.04
	CGCaP	186±15	0.95±0.02	167±26	0.93±0.02

*Statistical comparisons of $p<0.05$ between CGCaP zone and both the CG and interface zones fabricated at −10 °C.

Table 3

Linear elastic moduli (E^*) as well as collapse strain ε^*_{el} and stress σ^*_{el} of CG, 80 wt% CGCaP, and 80 wt% CG–CGCaP I scaffolds. Results reported as a function of final freezing temperature with mean ±STD,n = 6.

		E^* (kPa)		ε^*_{el}		σ^*_{el} (kPa)	
		T_f−10 °C	T_f−40 °C	T_f−10 °C	T_f−40 °C	T_f−10 °C	T_f−40 °C
Si	CG	8.8±1.1	8.1±0.4	0.09±0.06	0.14±0.04*	0.7±0.4	0.9±0.3
	CGCaP	159.0± 18.3**	123.4± 11.3**§	0.09± 0.05	0.07± 0.03	11.2± 2.5**	7.5± 2.0**§
Multi		22.5±1.1*	18.9±3.2	0.11±0.04	0.13±0.02*	2.1±0.8	2.1±0.2

*Statistical comparison of $p < 0.05$ between multi-compartment CG-CGCaP and CG scaffold variants.

**Statistical comparison of $p < 0.05$ between mineralized CGCaP and CG scaffold variants.

§Statistical comparison of $p < 0.05$ between solidification temperatures for a given variant.

Table 4

Permeability of the single-compartment CG and 80 wt% CGCaP scaffolds (ε:0% strain), mean±STD n = 3

		Permeability (m^2)	
		T_f−10 °C	T_f−40 °C
Single	CG	$2.4\pm0.5\times10^{-8}$*	$1.6\pm0.1\times10^{-8}$§
	CGCaP	$6.1\pm1.4\times10^{-7}$	$3.7\pm0.4\times10^{-7}$§
Multi		$5.7\pm0.9\times10^{-9}$	$1.4\pm0.3\times10^{-8}$§

* $p<0.05$ vs. CGCaP scaffold (statistical comparison between scaffold type at each fabrication temperature).

§ $p<0.05$ vs. T_f−10 °C for each scaffold variant (statistical comparison between fabrication conditions for each type of scaffold).